

Functional Assessment of Hand Vasculature Using Infrared and Laser Speckle Imaging

A.M. Gorbach¹, H. Wang¹, B. Wiedenbeck¹, W. Liu², P.D. Smith¹, and E. Elster²

¹National Institute of Biomedical Imaging and Bioengineering, NIH, Bethesda, USA,
gorbach@helix.nih.gov; ²Naval Medical Research Center, USA

ABSTRACT

To assess vascular responses of the human hand to inspiratory gasps and hand cooling, two imaging “remote sensing” instruments were utilized: 1) a high-resolution infrared (IR) imaging camera and 2) a full-field laser perfusion imager (FLPI). Data analysis was performed on the data sets collected simultaneously from both instruments.

A non-localized drop of both FLPI and IR signals was observed at ~0.5-2.0 min after gasp onset. Spontaneous oscillations, much below the human cardiac and respiratory frequencies, were observed with both imagers. The dominant oscillations for both imaging modalities centered around 0.01Hz. Spectral frequencies, their power, and the duration of temperature oscillations (bursts) for different hand areas changed in time and were spatially heterogeneous. The highest spatial correlation between the two data sets was found between the mean IR derivative image and the mean original FLPI image for the baseline conditions. Heterogeneous images of the human hand were consistently detected non-invasively by both instruments. After cooling, a temperature elevation of ~0.5°C was seen as a spotted pattern mainly in the thenar and hypothenar areas. A generalized increase in perfusion over the same areas was observed in FLPI images.

Both IR and FLPI imagers sensitively identify vasoconstrictor responses induced by inspiratory gasp and hand cooling maneuvers. The specificity to physiological changes and high imaging rate for both instruments, coupled with the current ease of use of optical cameras in clinical settings, make the described combination of two instruments an ideal imaging approach to studying the dynamics of thermal and perfusion heterogeneity in human skin.

KEYWORDS: Infrared imaging, laser speckle imaging, vasomotion, temperature regulation, human hand, arterio-venous anastomosis.

I. INTRODUCTION

Current knowledge of thermal regulation in humans is based mainly on data acquired by point probes. Some require physical contact with the tissue under investigation, or are even invasive, thus potentially introducing bias into the measurement. Such approaches can limit understanding of the spatial extent and functional involvement of multiple distributed vascular structures in the human body. In particular, a unique vascular structures—arterio-venous anastomosis (AVAs)—lying about ~ 4 mm beneath the surface of the palms regulate a large volume of blood over a two dimensional plane [1]. Characterization of the subcutaneous AVAs has been limited mainly to their anatomical description [1], to experimental observation of their synchronous vasomotion under baseline conditions [2] and to their involvement in regulation of blood flow in the digits during cold stress [3]. Identification of AVA encapsulated structures, their number, and the functional relationships between them may have a profound effect on the delineation of the vascular regulation of blood flow and thermoregulation in humans. To address these issues, we attempted to apply two “remote sensing” imaging instruments to locate AVAs as they actively functioned, and to assess related temperature and perfusion fluctuations in the human hand.

II. METHODS

A high-resolution infrared (IR) imaging camera (Lockheed Martin, USA) and full-field laser perfusion imager (FLPI, Moor Instruments Ltd., England) were utilized to assess hand temperature and vascular perfusion, as well as their fluctuations during two experimental conditions. In experimental condition 1, a palm of each of 4 healthy volunteers was imaged with both cameras 20 min before, during, and 20 min after a 20-sec deep inspiratory gasp. In experimental condition 2, the palm of each of 20 volunteers was imaged with the IR camera (also with FLPI in four of the volunteers) 20 min before and 20 min after 2-min of cooling of the hand by immersion in $\sim 17^\circ\text{C}$ water. Both cameras were directed toward the palmar surface of the right hand from ~ 30 cm away. IR images (2 Hz frame rate, 640×512 pixels per image) and FLPI images (5 Hz frame rate, 152×113 pixels per image) were acquired concurrently in experimental condition 1. In experimental condition 2, different acquisition parameters for the IR camera (5 Hz frame rate, 320×256 pixels per image) and FLPI images (1 Hz frame rate, 760×568 pixels per image) were utilized.

The following approach was designed for analysis of the two simultaneously collected data sets in experimental condition 1:

(A) IR images and FLPI images were aligned to remove motion artifacts and then co-registered. An image alignment algorithm was iteratively applied to different sets of fiduciary points within each image until it showed well aligned final IR and FLPI imaging sets.

(B) Temperature profiles (IR intensity vs. time) and perfusion profiles (FLPI intensity vs. time) were obtained for the same regions-of-interest (ROIs): 1) the entire hand and 2) tip of ring finger (ROI: 3×3 pixels) within each aligned frame of the two original sets.

(C) The derivative for each original temperature and perfusion profile was approximated using the following formula: $y'(t) = [y(t + h/2) - y(t - h/2)] / h$, where step size $h = 4$ sec and two new derivative imaging sets, one for IR and one for FLPI, were synthesized.

(D) Spectral analysis was applied to both original and derivative profiles to identify the frequencies of fluctuation of temperature and perfusion, and their derivatives, as well as their power magnitudes for the 20-min baseline condition. A first order polynomial de-trending algorithm (ENVI/IDL software) was applied to remove trends that might be present across successive images. A power spectrum was calculated by applying a Fast Fourier Transformation (FFT), with a window length = 250 seconds, to each of the original and derivative profiles. Using calculated power magnitudes at 0.008Hz, four total power spectrum images were synthesized: one for each of the original and derivative data sets. This frequency was chosen because 0.008 Hz oscillations showed the largest spectral power magnitudes.

(E) The continuous Morlet Wavelet Transform (CMWT) method was utilized to calculate the time-varying spectral features of the signals extracted from both original and derivative temperature and perfusion profiles with a 3×3 smoothing window.

The continuous Morlet wavelet transform of a signal $x(t)$ is defined by

$$X(\omega, t) = \int_{-\infty}^{\infty} \Psi_{\omega, t}(u) x(u) du, \quad (1)$$

where Ψ represents the Morlet window function.

For each time t_n and frequency ω_k , the complex value of wavelet transform $X(\omega_k, t_n)$ is obtained as

$$X(\omega_k, t_n) = a_{k,n} + ib_{k,n}. \quad (2)$$

The wavelet spectral magnitude may then be calculated as

$$SP_{k,n} = |X(\omega_k, t_n)|^2 = a_{k,n}^2 + b_{k,n}^2 \quad (3)$$

and the phase of the particular frequency is determined by

$$\phi_{k,n} = \arctan(b_{k,n} / a_{k,n}). \quad (4)$$

For two signals, $x_1(t)$ and $x_2(t)$, the relative phase difference $\Delta\phi_{k,n} = \phi_{2k,n} - \phi_{1k,n}$ can be computed.

The continuous wavelet spectrum was visualized as a *2D wavelet plot*, reflecting fluctuations of multiple frequencies (y-axis as a log scale) and their spectral powers (color pixels, log scale) over time (x-axis) for the chosen ROI (Fig. 2). A

total of four plots for the two modalities were used for further analysis: *2D wavelet plots* generated from original sets, and *2D derivative wavelet plots*, generated from synthesized derivative sets.

(F) Correlation analysis was performed using a *mean IR intensity* image and *mean FLPI intensity* image calculated from the original, aligned and co-registered, IR and FLPI sets. Similarly, a *mean IR derivative* image and *mean FLPI derivative* image were calculated from the synthesized IR and FLPI derivative sets for correlation analysis.

To quantify the IR and FLPI relationships in the spatial domain, correlation coefficients were calculated between IR images (variously the *mean intensity* image, *mean derivative* image, *spectral* image, and *derivative spectral* image) and the same type of FLPI images.

To quantify the IR and FLPI relationships in the time-frequency domain, correlation coefficients were calculated between IR-derived and FLPI-derived *2D wavelet plots* and *2D derivative wavelet plots*.

The correlation coefficients between the two modalities of images and plots were calculated by the following equation:

$$S = \frac{\sum_{(x,y) \in C} [I_1(x,y) - \overline{I_1(x,y)}] * [I_2(x,y) - \overline{I_2(x,y)}]}{\sqrt{\sum_{(x,y) \in C} [I_1(x,y) - \overline{I_1(x,y)}]^2 * \sum_{(x,y) \in C} [I_2(x,y) - \overline{I_2(x,y)}]^2}} \quad (5)$$

where I_1 , I_2 are intensities of the two images or plots respectively, and C is the mask of the image.

(G) Time-averaged Wavelet Phase Coherence (TWPC) was calculated to quantify the coherence among the IR, IR derivative, FLPI and FLPI derivative profiles for the chosen ROI. TWPC [4] was calculated as

$$C_\phi(\omega_k) = \sqrt{\overline{\cos(\Delta\phi_{k,n})}^2 + \overline{\sin(\Delta\phi_{k,n})}^2} \quad (6)$$

where $\overline{\cos(\Delta\phi_{k,n})}$ is the mean of $\cos(\Delta\phi_{k,n})$ and $\overline{\sin(\Delta\phi_{k,n})}$ is the mean of $\sin(\Delta\phi_{k,n})$.

For experimental condition 2, steps A, B, and D were performed, and the following was added:

(H) Mean images were calculated separately for the before- and after-cooling sessions by averaging each pixel's value across the entire session. These two mean images were subtracted to determine the average difference in flux or temperature between the two sessions.

Additional experiments and calculations were conducted to minimize the potential impact of 1/f noise related to the IR and FLPI instruments. Images of a black body calibration source (for IR calibration) and a suspension of polystyrene micro-spheres in water, undergoing Brownian motion, (for FLPI calibration) were collected and analyzed using the described procedure developed for the original data sets.

These IR and FLPI spectral magnitudes, for each frequency, were chosen as a lower threshold to eliminate 1/f noise and other radiation effects.

III. RESULTS

White noise was found in the signals measured from the black body calibration source for IR, and 1/f characteristic noise was found in the FLPI calibration signals. Log-log power spectra showed, for a central frequency of ~0.01 Hz, that both noise types were ~100 times smaller than observed IR and FLPI signals from the skin.

By analyzing temperature and perfusion profiles from the same ROI (Fig. 1), during experimental condition 1 with deep inspiratory gasps, we observed that reductions in FLPI preceded reductions in temperature by 20-100 sec.

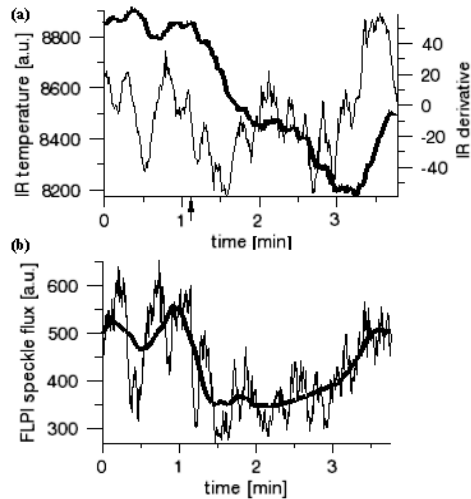


Fig. 1. (a) IR temperature profile (bold line) and its derivative (thin line). Arrow indicates start of 20-sec deep inspiratory gasp. (b) FLPI profile (thin line) and its trend (bold line). Note that the lowest FLPI trend (b, bold line) occurred ~0.5 min after the onset of the gasp. This preceded the lowest temperature, which didn't occur until ~2.0 min after the start of the same inspiratory gasp.

2D wavelet spectral plots for both modalities in experimental condition 1 showed the relationship between oscillation spectral powers (in color), frequencies, and time (Fig. 2) for the baseline condition. Burst-type changes for the temperature (Fig. 2a), its derivative (Fig. 2b), and the FLPI perfusion signal (Fig. 2c) were revealed. A heterogeneous spatial distribution of different frequency components and their dynamics was found with wavelet analysis for different ROIs and was characteristic for both IR and FLPI data sets.

For the tip of the ring finger ROI, the correlation in time frequency domain between FLPI- and IR-derived *2D wavelet plots* (see Fig. 2; frequency range 0.006 – 0.05 Hz; time duration 20 min) was found to be 0.67 and 0.69 - (see Table I).

TABLE I
Correlation coefficients in time/frequency domain (finger tip ROI)

		2D wavelet plot for IR	
		intensity	derivative
2D wavelet plot for FLPI	intensity	0.67	0.69
	derivative	-0.12	0.21

Table II presents the correlation coefficients for the spatial domain images shown in Fig. 3. Figs. 3a and 3e are the mean intensity images averaged over the whole time collection window for IR and FLPI images. Figs. 3b and 3f are the equivalent power spectrum images obtained at 0.008Hz. Figs. 3c and 3d are the synthesized derivative images of Figs. 3a and 3b. A correlation between *mean intensity* images for FLPI and IR in experimental condition 1 was only -0.06 and a correlation of 0.61 was found between FLPI and IR *mean derivative* images. A correlation of 0.57 was found between IR and FLPI spectral images and a similar correlation 0.58 was found between the *mean intensity* FLPI image and the IR *spectral* image.

TABLE II
Correlation coefficients in spatial domain (whole hand ROI)

		IR images			
		Mean intensity	Mean derivative	Spectrum	Derivative spectrum
FLPI images	Mean intensity	-0.06	0.61	0.58	0.42
	Mean derivative	0.04	0.13	0.16	0.18
	Spectrum	-0.28	0.49	0.57	0.59
	Derivative spectrum	-0.24	0.48	0.5	0.50

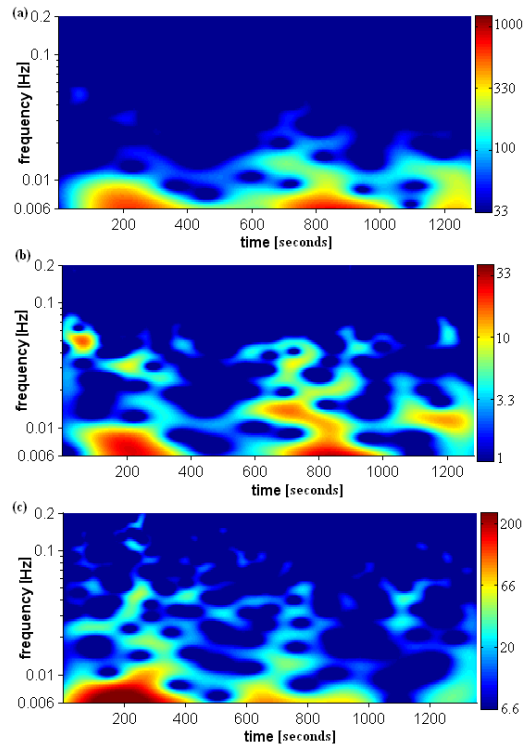


Fig. 2. Experimental condition 1: 2D Continuous Wavelet Plots for (a) IR signal, (b) derivative of IR signal, and (c) FLPI signal. The same ROI (3x3 pixels at finger tip) was used for these plots. The same analysis showed a similarity in existence of multiple frequency components related to vasomotion in the range between 0.008 Hz and 0.2 Hz.

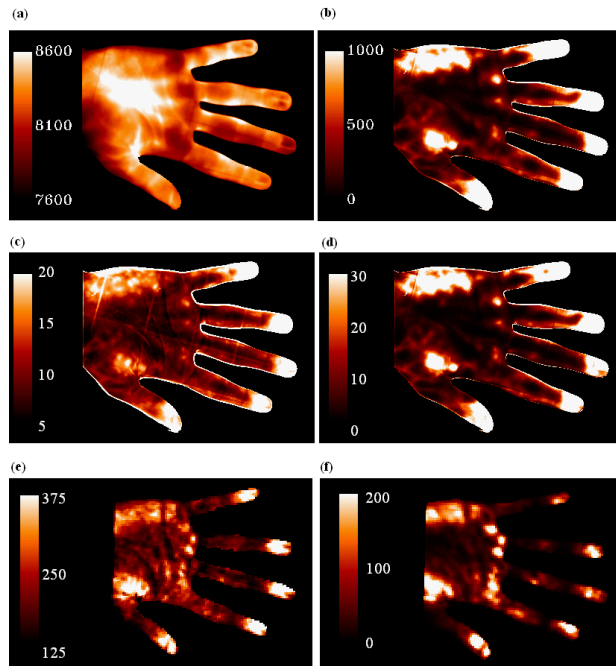


Fig. 3. Experimental condition 1: Examples of (a) mean IR intensity image, (b) IR spectral image, (c) mean IR derivative image, (d) IR derivative spectral image, (e) mean FLPI intensity image, and (f) FLPI spectral image.

Computed for the same ROI, the TWPC between two comparable data profiles (IR vs. FLPI original profiles, IR derivative vs. original FLPI profiles, original IR vs. derivative FLPI profiles, and derivative IR vs. derivative FLPI profiles) was found to be essentially the same, with the highest value (0.92) for the oscillation of ~ 0.01 Hz. There was a lesser value of 0.68 for 0.04 Hz oscillations (Fig. 4).

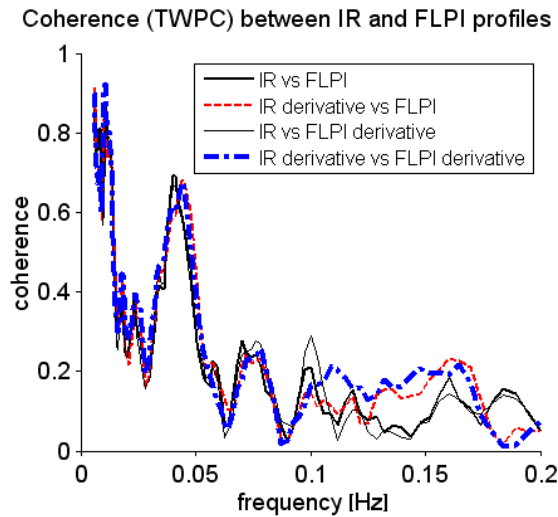


Fig. 4. TWPC between two comparable data profiles (IR vs. FLPI original profiles, IR derivative vs. original FLPI profiles, original IR vs. derivative FLPI profiles, and derivative IR vs. derivative FLPI profiles).

A low-density pattern of irregular spots (25-60 spots/palm) possessing increased temperature ($\sim 0.5^{\circ}\text{C}$ above surroundings) was observed on the IR images for experimental condition 2 (Fig. 5a) in the thenar and hypothenar palm areas during the first minute following hand cooling. The location of these spots varied from subject to subject, but was reproducible when measured multiple times in the same volunteer; the time for which spots remained visible varied between individuals and sessions. A generalized increase in perfusion over these areas could be observed in FLPI images, but the spots observed in IR images did not appear. However in mean-subtraction FLPI images, a high-density pattern of finer spots (Fig. 5b) with increased perfusion was observed in the same palm areas in two studies of the same patient. Similar mean-subtraction analysis performed on IR images had little effect on appearance of the low-density spots.

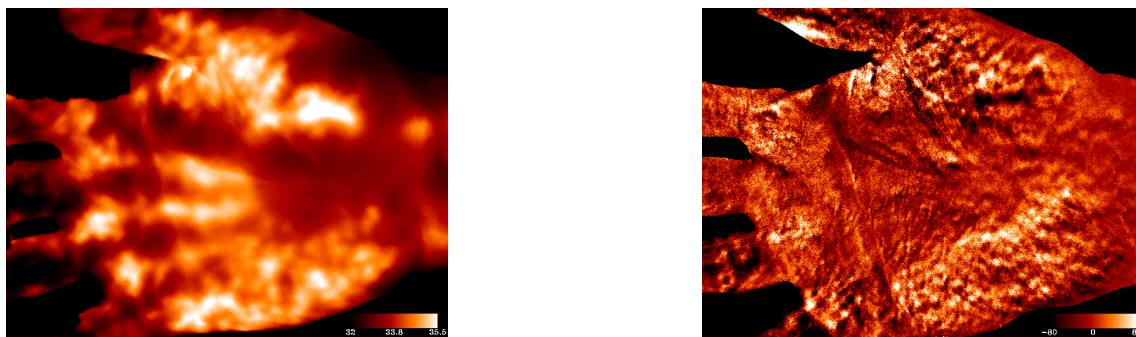


Fig. 5. Experimental condition 2: IR (a) and FLPI (b) mean-subtraction images of human palm registered during re-warming of the hand. Left: mean IR image before cooling subtracted from mean IR image after cooling. Right: mean FLPI image before cooling subtracted from mean FLPI image after cooling.

Normalized power spectra for baseline before and after cooling showed the same dominant frequency oscillations (~ 0.01 Hz) for two instruments (Fig. 6). Power spectra were calculated for 20 min before and 20 min after hand cooling.

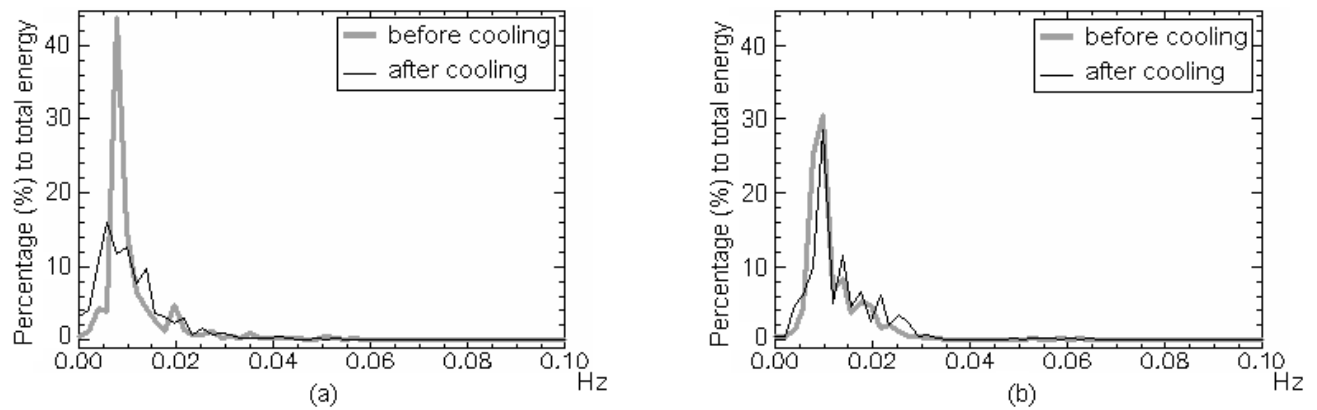


Fig. 6. Experimental condition 2: Example of normalized power spectra plots for (a) IR signal, and (b) FLPI signal. The whole palm ROI was used for these plots.

IV. DISCUSSION

The two instruments used in this study have different principles of measurement. FLPI [7, 8] uses the fact that highly perfused tissue produces rapid variations in laser speckle patterns (typically using irradiation with a 785 nm laser scanning source), which after integration by the CCD produces an area of low contrast. Conversely, low perfusion causes little variation in the speckle pattern and results in a high contrast area of well-defined speckle in the video image. The contrast is quantified and the resulting flux is color-coded to produce a perfusion image of the tissue surface. The signal from the IR camera is sensitive to IR emission at the measured wavelength ($3\text{--}5\ \mu$) and is directly proportional to temperature [5, 6]. The camera has a sensitivity of 0.02°C . We have previously shown that tissue perfusion can be quantified, and IR can be used to assess intraoperative cerebral perfusion [7, 8] and to provide real-time assessments of whole kidney reperfusion during renal transplantation [9]. However, thermal images are sensitive not only to blood flow, but also to metabolic heat [10].

This methodological study in healthy subjects showed that both IR and FLPI imaging sensitively and immediately identify vasoconstrictor responses induced by inspiratory gasp and hand cooling maneuvers. Spectral validation of the two instruments with calibration sources allows us to confidently talk about the principal findings, in experimental condition 1, of temperature and blood perfusion fluctuations: (1) Individual FLPI perfusion time profiles were correlated with the derivative of IR temperature profiles. (2) Spontaneous oscillations in temperature and perfusion during baseline conditions were consistently detected non-invasively by two independent instruments. These oscillations are much below the cardiac and respiratory frequencies for the human body. (3) The dominant peak of oscillations is centered around 0.01 Hz. (4) Spectral frequencies, their power, and duration of temperature oscillations (bursts) for different hand areas change in time and are spatially heterogeneous. (5) The highest correlation between two data sets was found between the mean IR derivative images and the mean original FLPI images for baseline conditions.

The penetration depth of the FLPI laser is enough to interrogate underlying blood flow to a depth between 0.4 mm and 0.9 mm [11, 12]. For human palm vasculature that depth would coincide with the epidermal layer and upper segments of the papillary loops [1]. These highly packed loops, consisting of an ascending arterial limb and a descending venous limb in a papilla, arise from and drain into the subpapillary arterial and venous plexi, respectively and nourish the avascular epidermis [1]. We suspect high-density spots observed with FLPI (mean-subtraction images) in experimental condition 2 during hand rewarming (Fig. 5b) in the thenar and hypothenar areas of the palm may be a reflection of these perfused papillary loops.

Our experiences with IR imaging in surgery, as well as physical modeling of IR sensitivity to perfused vessels at different depths [6], confirm that IR assessment provides deep tissue interrogation. Analysis of neurovascular features of the human palm suggests that high-density temperature clusters observed in IR images are a reflection of AVAs (glomi) located 3-4 mm deep in the reticular layer of the dermis of glabrous skin of the palm [1]. A glomus is a special pattern of arterio-venous shunt (or bypass) found in palmar skin (Fig. 7) and is believed to be heavily involved in regulation of temperature. The glomus is innervated by non-myelinated sympathetic nerve fibers. When glomus cells contract, the arterio-venous bypass is shut and blood flows into the capillary bed. The skin surface becomes warm, thus increasing heat loss. When the cells dilate, the arterio-venous bypass opens and the skin becomes cool, decreasing heat loss [1].

During the re-warming observed in experimental condition 2, the subpapillary arterial venous plexus is collapsed by cooling [3], probably making perfused glomi more “visible” for IR at the beginning of re-warming (~0.5-2 min after cooling offset). At latter stages of re-warming, the whole hand warmed and glomi were not seen by IR. FLPI images showed multiple high-density small clusters of increased perfusion, probably reflecting recovered flow in papillary loops.

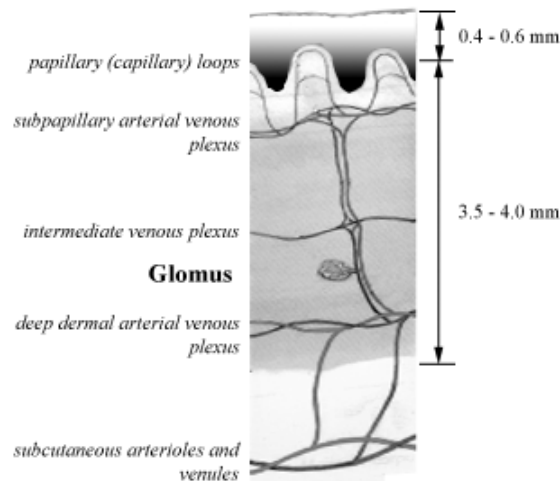


Fig. 7. Schematic representation of neurovascular features of glabrous skin. Note location of papillary loop beneath epidermis (0.4-0.6 mm thickness) and location of Glomus capsule in the reticular layer of dermis between deep dermal the arterio-venous plexus and intermediate venous plexus. The thickness of dermis for glabrous skin is 3.5-4.0 mm.

Experimental and clinical findings suggest that observed blood flow oscillations are dependent on spontaneous activity of the microvessel smooth muscle cells, local sympathetic activity and microvascular endothelial activity [13, 14]. Based upon these findings, we suggest that a combined IR and FLPI technique, coupled with spatial and time-frequency domain analysis, might be useful in identifying individual regulators of blood flow within the skin vessel plexi and reflect their vasoregulatory efficiency.

V. CONCLUSIONS

With rewarming-enhanced IR imaging, the location and functionality of AVAs in the human palm can be characterized. The location and status of blood flow in papillary loops can be characterized with FLPI imaging of the human palm.

Specificity to physiological changes and a comparatively high imaging rate for both instruments (up to 25 Hz), coupled with the current ease of use of optical cameras in clinical settings, suggest that the described combination of two instruments is an viable imaging approach to studying heterogeneity of microvasculature and its rhythmicity in the human hand without the introduction of contrast agents. When the two instruments are used for tissue assessment, observed differences might be explained by the reduced penetration depth of the FLPI compared with IR interrogation depth.

ACKNOWLEDGMENT

This research was supported, in part, by the Intramural Research Program of the NIBIB, NIH and the Naval Medical Research Center.

The views expressed in this article are those of the author and do not necessarily reflect the official policy or position of the Department of the Navy, Department of Defense, nor the U.S. Government. This work was supported by funded by work unit number: 602227D.0483.01.A0518 (MFEL). I am a military service member (or employee of the US Government). This work was prepared as part of my official duties. Title 17 U.S.C. 105 provides that 'Copyright protection under this title is not available for any work of the United States Government.' Title 17 U.S.C. 101 defines a U.S. Government work as a work prepared by a military service member or employee of the US Government as part of that person's official duties.

VI. REFERENCES

- [1] Yu, H., Chase, R., and Strauch, B., [Atlas of hand anatomy and clinical implications], Mosby, 559 (2004).
- [2] Bergersen, T.K., "A search for arteriovenous anastomoses in human skin using ultrasound Doppler," *Acta Physiol Scand*, 147(2), 195-201(1993).
- [3] Bergersen, T.K., Eriksen, M., and Walloe, L., "Local constriction of arteriovenous anastomoses in the cooled finger," *Am J Physiol*, 273(3 Pt 2), R880-6 (1997).
- [4] Bandrivskyy, A., et al., "Wavelet phase coherence analysis: application to skin temperature and blood flow," *Cardiovascular Engineering: An International Journal*, 4(1), 89-93 (2004).
- [5] Gorbach, A.M., et al., "Intraoperative infrared functional imaging of human brain," *Ann Neurol*, 54(3), 297-309 (2003).
- [6] Ivanitsky, G.R., et al., "Display peculiarities of hypodermic heating sources on the human body surface," *Dokl Biochem Biophys*, 420, 130-4 (2008).
- [7] Watson, J.C., et al., "Real-time detection of vascular occlusion and reperfusion of the brain during surgery by using infrared imaging," *J Neurosurg*, 96(5), 918-23 (2002).
- [8] Gorbach, A.M., et al., "Intraoperative infrared imaging of brain tumors," *J Neurosurg*, 101(6), 960-9 (2004).
- [9] Gorbach, A., et al., "Objective, real-time, intraoperative assessment of renal perfusion using infrared imaging," *Am J Transplant*, 3(8), 988-93, (2003).
- [10] Gorbach, A.M., Wang, H. and Elster, E., "Thermal oscillations in rat kidneys: an infrared imaging study," *Philos Transact A Math Phys Eng Sci*, 366(1880), 3633-47 (2008).
- [11] Ruth, B., "Measuring the steady-state value and the dynamics of the skin blood flow using the non-contact laser speckle method," *Med Eng Phys*, 16(2), 105-11 (1994).
- [12] Li, N., et al., "High spatiotemporal resolution imaging of the neurovascular response to electrical stimulation of rat peripheral trigeminal nerve as revealed by in vivo temporal laser speckle contrast," *J Neurosci Methods*, (2008).
- [13] Kvandal, P., et al., "Low-frequency oscillations of the laser Doppler perfusion signal in human skin," *Microvasc Res*, 72(3), 120-7 (2006).
- [14] Rossi, M., et al., "Skin vasomotion investigation: a useful tool for clinical evaluation of microvascular endothelial function?" *Biomed Pharmacother*, 62(8), 541-5 (2008).